# Theoretical analysis of scalar relaxation in $^{13}$C-DNP in liquids

Tomas Orlando [*],[a], Ilya Kuprov [b], Markus Hiller [a]

[a] *ESR Spectroscopy Group, Max Planck Institute for Multidisciplinary Sciences, Göttingen, Germany*
[b] *School of Chemistry, University of Southampton, Southhampton, United Kingdom*

## ABSTRACT

Dynamic nuclear polarization in the liquid state via Overhauser effect is enabled by the fluctuations of the electron-nuclear hyperfine interaction. Fermi contact (or scalar) hyperfine coupling can be modulated by molecular collisions on timescales of a few picoseconds and shorter, enabling an effective polarization transfer even at high magnetic fields. However, only a few studies have presented a theoretical analysis of the scalar mechanism. Here we report the current understanding of the scalar relaxation in liquid-state DNP and present different modeling strategies based on analytical relaxation theory and numerical calculations from molecular dynamics simulations. These approaches give consistent results in identifying the timescale of the fluctuations of the scalar interaction that drives $^{13}$C-DNP in the model system of CHCl$_3$ doped with nitroxide radical. Subpicosecond fluctuations arise not only from random molecular collisions but are also present when target molecule and polarizing agent form a transient complex that persists for tens of picoseconds. We expect that these kind of interactions, possibly based on hydrogen bond-like complexations, might be present in a large variety of compounds.

## 1. Introduction

Since the early developments, NMR spectroscopy has been hampered by its low sensitivity caused by the small energy gap between the nuclear Zeeman levels in a magnetic field. The small nuclear polarization often prevents NMR experiments on low gamma nuclei, low abundant isotopes, low concentration samples, or samples that are scarce or available in small amount. The sensitivity issue was tackled by developing hyperpolarization methods that increase NMR signals by orders of magnitude [1,2]. Among those, dynamic nuclear polarization (DNP) is currently one of the most popular: it relies on the transfer of polarization from unpaired electrons spins to the nuclei enabled by microwave irradiation.

In solids, DNP is extremely effective. Three different physical mechanisms (solid effect, cross effect, and Overhauser effect), which require different matching conditions, are active [3,4]. DNP allows the polarization to be transferred from a polarizing agent (usually a radical or a metal ions) via microwave irradiation to a target molecule. Eventually, NMR signals are enhanced by more than 100-fold [5]. The ongoing optimization of hardware, polarizing agents, and detection schemes has made DNP-NMR in the solid-state a unique tool to save experimental time and enable new science [5,6].

The situation is different in the liquid-state, where DNP is not yet a mature methodology to be broadly applied to high-resolution NMR spectroscopy. The reason is twofold. On the one hand, there are technical challenges when designing double resonance probes where efficient microwave irradiation, large sample volumes, and state-of-the-art NMR resolution coexist [7]. New developments in this direction showed that it is possible to mitigate sample heating [8,9], or use large samples volumes [10,11], or keep a good NMR resolution[12,13], but it has not been proven yet that these solutions can be implemented all at once in a single probehead.

On the other hand, the physical mechanism that governs the polarization transfer is in many cases strongly field dependent [14]. This is often the case if $^1$H is chosen as the target nucleus for DNP: enhancements $\epsilon$ are usually negative, and the highest values obtained in H$_2$O doped with nitroxide radicals are $\sim -160$ at 3.4 T [15] and $\sim -80$ at 9.4 T [16], both recorded close to the water boiling point. For a liquid at room temperature and ambient pressure, it has been shown experimentally and theoretically that at magnetic fields up to 1 T the maximum $^1$H enhancement is $\epsilon \sim -10^2$, but it drops to $\sim -10$ at 9.4 T [7,14,17]. This makes DNP unattractive at magnetic fields that are interesting for high-resolution NMR spectroscopy.

However, this limitation does not hold if other target nuclei, such as $^{13}$C, $^{19}$F, $^{31}$P, are chosen. In those cases, the enhancements in liquids at ambient temperature and pressure are positive—indicating a different mechanism—and still sizable at magnetic fields >3 T: +20-fold on $^{19}$F at 5 T [18], +600-fold on $^{13}$C at 9.4 T [13], +160-fold on $^{31}$P at 14.1 T [11] are, among others [10,12,19,20], some of the largest values reported so far.

These differences between $^1$H-DNP and DNP to other nuclei are

---

related to the physical processes responsible for the polarization transfer [21]. The Overhauser effect is the sole active mechanism in DNP in the liquid state when using organic monoradicals as polarizing agents, although recently new mechanisms have been theoretically investigated for biradicals in solutions [22,23]. The Overhauser effect is based on electron-nuclear cross-relaxation that originates from the fluctuations of both the dipole-dipole and the scalar (Fermi contact) hyperfine coupling. The cross-relaxation, and ultimately the electron-nuclear polarization transfer, has a maximum efficiency when such fluctuations are modulated close to the electron Larmor frequency ($\omega_e \tau \sim 1$, where $\tau$ is the correlation time of such fluctuations). If the Overhauser effect originates exclusively from electron-nuclear magnetic dipole-dipole interactions, a process modulated by molecular diffusion (translational or rotational) and active on a timescale of tens of picoseconds, the polarization transfer efficiency decreases rapidly with the magnetic field.

On the contrary, the scalar coupling is modulated by molecular collisions and can happen on a much faster timescale: this means that, in standard solvents, this process has $\tau < 10$ ps and, in the most favorable cases, even $\lesssim 1$ ps [13,20,24]. Importantly, the two mechanism are counteractive, and only if the scalar coupling dominates over the dipolar one the DNP can be efficient at high magnetic field (if $\tau \sim 1$ ps, $\omega_e \tau \sim 1$ for B $\sim 4$ T). While the dipolar interaction is ubiquitous and often dominates the electron-nuclear hyperfine coupling (as in the case of $^1$H-DNP), large electron-nuclear scalar couplings, which require a delocalization of the electron spin density to the target nucleus position [25], are less common.

Earlier studies suggest that enhancements driven predominantly by scalar interaction are common for $^{19}$F [18,26], although this strongly depends on the organic radical chosen as a polarising agent [19,26]. $^{31}$P shows large scalar enhancements at high magnetic fields, but it has been tested only in its trivalent form [10,11]. For $^{13}$C, scalar enhancements are more frequently observed in the presence of halogens [27,28], and compounds like $^{13}$CHCl$_3$ and $^{13}$CCl$_4$ are very favorable cases [20,29,30]. At low fields, a weakly acidic complexation interaction between target molecule and nitroxides can also favor the scalar interaction [30]. Surprisingly, enhancements $\epsilon > 15$ have been observed at high magnetic fields (9.4 T) in non-halogenated molecules such as diethyl malonate, ethyl acetoacetate, pyruvic acid [13,20], and phenylacetylene [12] and, more recently, in amino acids dissolved in water, where an hydrogen bond complexation with the radical is present [31]. The variety of these results obtained over four decades and the scarcity of studies at high magnetic fields conveyed the idea that a scalar interaction capable of driving large enhancements occurs only in exceptional cases [23]. This conclusion was further strengthened by the lack of a reliable strategy to predict the scalar enhancements that could be expected for different polarizing agents and different solvents.

In this contribution, we report a description of the current understanding of the electron-nuclear scalar interaction that is relevant for DNP in the liquid state. We compare a phenomenological description based on semi-classical nuclear relaxation theory, calculations performed with Bloch-Redfield-Wangsness (BRW) relaxation theory [32, 33], and a numerical treatment based on molecular dynamics (MD) simulations. The methods are reviewed for the case of $^{13}$C-DNP in CHCl$_3$, which has been extensively studied experimentally in the last few years. Our results suggest that a sub-picoseconds modulation of the scalar interaction can exist even in the presence of a transient complexation between the radical and the target molecule possibly enabled by hydrogen-bond like interactions. We show that the three modeling methods can describe the collisional nature of this dynamics and can identify the characteristic timescales of the fluctuations of the scalar interaction.

## 2. Theory

The conventional description of the Overhauser effect starts with a two-spin system ($S = 1/2$ for the electron, and $I = 1/2$ for the nucleus) interacting via hyperfine coupling (Fig. 1a) [34]. The evolution of the populations of the four energy level is governed by Solomon equations [35]. When solved for the steady state corresponding to a CW irradiation on resonance with the $\Delta m_S = \pm 1$ transition, they yield the well-known Overhauser equation for the NMR enhancement $\epsilon$ [36]:

$$\epsilon = \frac{\langle I_z \rangle}{\langle I_z^{eq} \rangle} = 1 - \xi \cdot s \cdot f \cdot \frac{|\gamma_e|}{\gamma_n} \qquad (1)$$

where $\gamma_e$ and $\gamma_n$ are the gyromagnetic ratios of electron and nucleus, respectively; $s$ is the saturation factor, representing the deviation of the electron spin polarization from the equilibrium, i.e. $s = (\langle S_z \rangle - \langle S_0^{eq} \rangle)/\langle S_0^{eq} \rangle$; the leakage factor $f = R_{1,para}/(R_{1,para} + R_{1,dia})$ quantifies the amount of paramagnetic relaxation relative to the total nuclear relaxation. These two terms are $f \approx 1$ and $s \approx 1$ when the radical concentration is larger than a few mM, and when the electron spins are fully saturated with high-power microwave irradiation. Then, the achievable enhancements depend on the coupling factor $\xi$, which is a function of the cross-relaxation rates $w_0$ (zero-quantum) and $w_2$ (double-quantum) (Fig. 1):

$$\xi = \frac{w_2 - w_0}{w_2 + 2w_{1,I} + w_0} \qquad (2)$$

The cross-relaxation rates are determined by the fluctuations of the anisotropic (dipolar) and isotropic (scalar) hyperfine coupling between the electron and the nuclear spins that are modulated at frequencies close to the electron Larmor frequency $\omega_e/2\pi$. Following Solomon's treatment [35], the transition rates are functions of the spectral density functions (SDFs) associated with such fluctuations:

$$w_0 = k_D \cdot J_D(\omega_e, \tau_D) + k_{SC} \cdot J_{SC}(\omega_e, \tau_{SC}) \qquad (3)$$

$$w_2 = 6k_D \cdot J_D(\omega_e, \tau_D) \qquad (4)$$

where the subscripts 'D' and 'SC' indicate the dipolar and the scalar part, respectively. In particular, $J_D(\omega_e, \tau_D)$ is the SDF for dipolar coupling fluctuation with correlation time $\tau_D$, and $J_{SC}(\omega_e, \tau_{SC})$ is the SDF for the scalar part with correlation time $\tau_{SC}$. The constant $k_D$ is model dependent (Supplementary Information), while $k_{SC} = 2S(S+1)/3$ [37].

It is important to note that the fluctuations of the scalar hyperfine coupling drive only the zero-quantum transition $w_0$ (Eq. 3), while the
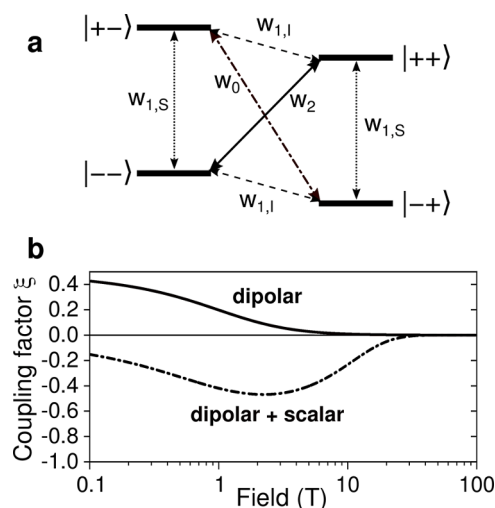


**Fig. 1. a)** Energy level diagram for two spins 1/2 interacting via hyperfine coupling. The states are indicated as $|m_S \, m_I\rangle$. **b)** Coupling factor as a function of the magnetic field calculated for $^{13}$C using a dipolar contribution with translational correlation time $\tau_D = 30$ ps, and using the same dipolar contribution plus a scalar one with $\tau_{SC} = 1$ ps.

dipolar part drives both $w_0$ and $w_2$. In other words, the scalar interaction and the dipolar one are counteracting terms and contribute with opposite signs to the DNP efficiency (Fig. 1b). This becomes clearer when rewriting Eq. 2 using Eqs. 3 and 4; the coupling factor $\xi$ as a function of the SDFs is then:

$$\xi = \frac{5k_D \cdot J_D(\omega_e, \tau_D) - k_{SC} \cdot J_{SC}(\omega_e, \tau_{SC})}{R_{1,para}} \,. \tag{5}$$

The paramagnetic relaxation term $R_{1,para}$ in the denominator can also be written as a function of the SDFs [37]

$$R_{1,para} = \begin{aligned} &7k_D J_D(\omega_e, \tau_D) + 3k_D J_D(\omega_n, \tau_{SC}) + \\ &+ k_{SC} J_{SC}(\omega_e, \tau_{SC}). \end{aligned} \tag{6}$$

Therefore, the coupling factor $\xi$ can be calculated when the SDFs are known.

In the context of DNP in the liquid state, the electron-nuclear dipolar interaction has been extensively investigated, because it is the dominant mechanism in $^1$H-DNP. The SDF $J_D(\omega, \tau_D)$ has been calculated both analytically (based on semi-classical nuclear relaxation theory) [37–39] and numerically, with molecular dynamics (MD) [40–42]. The two approaches are consistent in describing the diffusional dynamics governing the dipole-dipole interaction, as demonstrated by $^1$H-DNP studies in water [40] and toluene [41] doped with nitroxide radicals.

On the other hand, the scalar interaction is less well understood. The SDF for the scalar interaction $J_{SC}(\omega_e, \tau_{SC})$ has been modeled from DNP data at low fields ($< 0.34$ T) using a phenomenological approach [26]. The same analytical model has been recently extended up to 9.4 T [13, 20] and used to analyze the efficiency of different polarizing agents in $^{13}$C-DNP [24,25]. In parallel, Sezer and coauthors extended the MD-based numerical approach to calculate $J_{SC}(\omega_e, \tau_{SC})$ [43]. In the following, we describe three methods for obtaining the SDF for the scalar interaction.

*Semi-classical relaxation theory: the pulse model*

The semi-classical formulation of the electron-nuclear scalar interaction assumes $\tau_{SC} \ll T_{1,e}$, where $T_{1,e}$ is the longitudinal relaxation time of the electron. This condition defines the scalar relaxation of the first kind and is satisfied for most organic radicals in solution state ($T_{1,e} \sim$ 500 ns for nitroxides in organic solvents) [44,45]. In the semi-classical treatment [46], the stochastic nature of the fluctuations of $A_{iso}(t)$ is represented by Lorentzian SDF for the scalar interaction, i.e. $J_{SC}(\omega_e, \tau_{SC}) = \tau_{SC}/(1 + \omega_e^2 \tau_{SC}^2)$, which assumes an autocorrelation function consisting of a mono exponential decay [32].

This can be improved to better describe the evolution of $A_{iso}$ when an electron spin, localized on an organic radical molecule, interacts with a nuclear spin of a diamagnetic target molecule. In the context of the early application of DNP for studying liquid dynamics, Müller-Warmuth and coauthors introduced the "pulse model" to describe the electron-nuclear scalar interaction modulated by random molecular collisions [29,47]. In this framework, the time dependence of the isotropic hyperfine coupling is represented by a series of "pulses", each one of them corresponding to a collision between the molecules (Fig. 2). For each collision, $A_{iso} \neq 0$, meaning that the electron spin density is partly delocalized to the nucleus position, while $A_{iso} = 0$ when the two molecules are apart. The fluctuations of $A_{iso}$ is

$$A_{iso}(t) = \sum_{n=1}^{\infty} A_n \cdot s(t - t_n) \tag{7}$$

where $s(t - t_n)$ is the shape of the pulse, $t_n$ is the time point of the $n^{th}$ collision, and $A_n$ is the hyperfine coupling of the $n^{th}$ collision. Eq. 7 can be further extended when more than one type $i$ of pulses are present at the same time, representing, for instance, different geometries of the collision between radical and target molecule: $A_{iso}(t) = \sum_i A_{iso}^{(i)}(t)$. Fig. 2 shows a schematic representation of the pulse model with two types of pulses (collisions), the first with Lorentzian shape and width $2\tau_1$ and the second also with Lorentzian shape but a longer pulse duration $2\tau_2$.

For the pulse model, the SDF for the scalar interaction is obtained by Fourier transforming of the autocorrelation function $K(t) = \langle A_{iso}(\tau) \cdot A_{iso}(\tau + t) \rangle_\tau$. In the case of pulses with Lorentzian shape and correlation time $\tau_i$, i.e. $s(t) = \tau_i/(1 + t^{-2}\tau_i^2)$, the SDF is

$$\begin{aligned} J_{SC,Pulse}(\omega_e, \tau_i) &= \sum_i J_{SC,Pulse}^{(i)}(\omega_e, \tau_i) = \\ &= \sum_i \frac{4\pi^2 \langle A_i \rangle^2}{\tau_{p,i}} [\tau_i \cdot \exp(-\omega_e \tau_i)]^2 \end{aligned} \tag{8}$$

Here, $\omega_e$ is the electron Larmor frequency, $\tau_i$ is the half-width of the collision $i$, $\langle A_i \rangle$ is the average amplitude (in Hz), and $1/\tau_{p,i}$ is the frequency of the collisions of type $i$. The concentration of the radical is not explicitly included as a prefactor [48]. An example of an SDF calculated with Eq. 8 is shown in Fig. 2b, where two types of Lorentzian collisions are considered, with correlation times $2\tau_1 = 1$ ps and $2\tau_2 = 20$ ps, respectively. The SDF with shorter correlation time gives a significant contribution to the total SDF at electron Larmor frequencies $\omega_e/2\pi > 100$ GHz.

The SDF $J_{SC,Pulse}(\omega_e, \tau_i)$ changes when the pulse shape $s(t - t_n)$ in Eq. 7 is chosen differently. A few examples of $J_{SC,Pulse}(\omega_e, \tau_i)$ calculated for
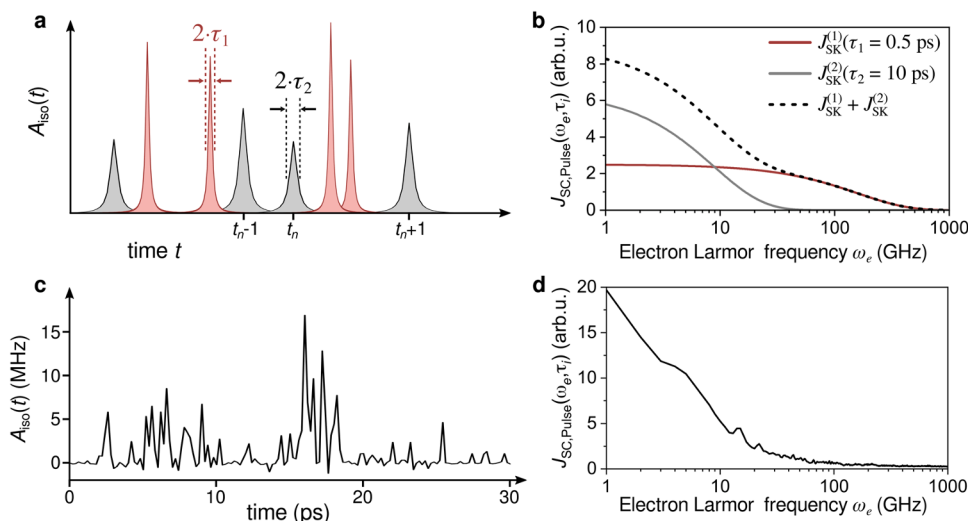


Fig. 2. a) Representation of the time fluctuation of the hyperfine coupling $A_{iso}(t)$, according to the pulse model for molecular collisions. Two types of collisions are shown, both having a Lorentzian pulse shape, but different collision duration, $2\tau_1$ and $2\tau_2$, respectively. b) SDFs calculated with the pulse model using two contributions: $J_{SC,Pulse}(\omega_e, \tau_1)$ [$\langle A_{iso} \rangle = 1.6$ MHz, $\tau_{p,1} = 10$ ps, $\tau_1 = 0.5$ ps] in red; and $J_{SC,Pulse}(\omega_e, \tau_2)$ [$\langle A_{iso} \rangle = 0.8$ MHz, $\tau_{p,1} = 50$ ps, $\tau_1 = 10$ ps] in gray. The sum of the two is shown as a dashed line. c) Example of $A_{iso}(t)$ obtained from numerical simulations (MD and DFT) for CHCl$_3$ molecule diffusing around TEMPONE radical (time resolution 0.2 ps). d) SDF computed from $A_{iso}(t)$ of the kind shown in panel c, extended for the range 0–1000 ps. (For interpretation of the references to colour in this figure legend, the reader is referred to the web version of this article.)

different shapes of the collision pulse (Lorentzian, Gaussian, and square) are shown in the Supplementary Information.

Finally, the contribution of the scalar relaxation to the nuclear relaxation can be calculated as [37]

$$R_{1,SC}^{(Pulse)} = \frac{2}{3} S(S+1) J_{SC,Pulse}(\omega_e, \tau_i) \,, \tag{9}$$

where $S$ is the electron spin quantum number.

*BRW relaxation theory: scalar relaxation of the first kind*

The cross-relaxation process can be treated using the Bloch-Redfield-Wangsness (BRW) relaxation theory [32,33]. In this framework, we consider a system containing an electron and a nuclear spin coupled via dipole-dipole and scalar interaction. The stochastic processes that modulate them (rotational diffusion and collisional dynamics) were assumed to be uncorrelated.

The dipole-dipole relaxation via rotational diffusion has been treated as described in the Supplementary Information. For the scalar coupling between the two spins, we consider collisional dynamics that modulate the hyperfine coupling and induces cross-relaxation via the scalar relaxation of the first kind [46]. In this case, the stochastic part of the hamiltonian can be written as [49]:

$$\widehat{H}_1(t) = a_1(t)\widehat{V} \tag{10}$$

where $\widehat{V} = \widehat{E}_X \widehat{N}_X + \widehat{E}_Y \widehat{N}_Y + \widehat{E}_Z \widehat{N}_Z$ (with $\widehat{E}$ and $\widehat{N}$ being the spin operators of electron and nuclei, respectively), and $a_1(t)$ is the time dependent part of the hyperfine coupling. The standard BRW relaxation theory treatment yields the relaxation superoperator [49]:

$$\widehat{\widehat{R}} = -\int_0^\infty \langle a_1(t)a_1(t-\tau)\rangle \widehat{\widehat{V}} e^{-i\widehat{\widehat{H}}_0\tau} \widehat{\widehat{V}} e^{+i\widehat{\widehat{H}}_0\tau} d\tau \,. \tag{11}$$

where $\widehat{H}_0$ is the static part of the Hamiltonian and $\langle a_1(t)a_1(t-\tau)\rangle$ is the autocorrelation function for the scalar interaction. The autocorrelation function can be expressed as a linear combination of exponential decays with weights $w_k$ and correlation times $\tau_{SC,k}$

$$\langle a_1(t)a_1(t-\tau)\rangle = \Delta_a^2 \sum_k w_k \exp\left(-\frac{\tau}{\tau_{SC,k}}\right) \tag{12}$$

where $\Delta_a$ is the modulation depth of the hyperfine coupling (in rad/s). With this expression, the cross-relaxation rate in presence of the sole scalar relaxation becomes [49,50]:

$$\begin{aligned} \sigma_{E,N} &= \frac{\langle \widehat{N}_z | \widehat{\widehat{R}} | \widehat{E}_z \rangle}{\sqrt{\langle \widehat{N}_z | \widehat{N}_z \rangle}\sqrt{\langle \widehat{E}_z | \widehat{E}_z \rangle}} = \\ &= \frac{\Delta_a^2}{2} \sum_k w_k \frac{\tau_k}{1 + \tau_{SC,k}^2(\omega_e - \omega_n)^2} \approx \\ &\approx \frac{2}{3}S(S+1)J_{SC,BRW}(\omega_e, \tau_{SC,k}) \,, \end{aligned}$$

where the last equality is analogous to Eq. 9 and considers $(\omega_e - \omega_n) \approx \omega_e$ [46,51]. The Lorentzian SDF $J_{SC,BRW}(\omega_e, \tau_{SC,k})$ is compatible with random fluctuation of the hyperfine coupling arising from a molecular complex formation [29]; in the following, we show that this can also describe collisional processes in liquids.

*Numerical Simulations of $A_{iso}(t)$*

The fluctuations of the isotropic hyperfine coupling $A_{iso}(t)$ depend on the molecular motions. Specifically, $A_{iso}$ is not zero when the two molecules are close enough to have an orbital overlap, i.e. a non-negligible electron spin density to the position of the target nucleus. As previously

reported [43], this process can be investigated numerically. Molecular dynamics (MD) simulation is used to compute the diffusion of one (or more) radical molecule(s) surrounded by solvent molecules, which usually carry the target nuclei of the DNP experiment. This allows to track the position of each solvent molecule diffusing around the radical molecule.

The electron-nuclear hyperfine coupling can then be estimated at each time point with density functional theory (DFT). In this way, one obtains the electron-nuclear hyperfine coupling as a function of time $A_{iso,m}(t)$ for each $m$-th target nucleus. As shown in Fig. 2c, $A_{iso,m}$ is the numerical counterpart of the analytical expression given by the pulse model in Eq. 7.

From the hyperfine traces $A_{iso,m}(t)$, one can derive the SDF [43,52]. The total autocorrelation function is defined as

$$\begin{aligned} K(t) &= \sum_m K_m(t) = \\ &= \frac{4\pi^2}{N} \sum_m \langle A_{iso,m}(\tau) \cdot A_{iso,m}(\tau + t)\rangle_\tau, \end{aligned} \tag{16}$$

where $N$ is the number of target nuclei per radical in the unit of volume (Supplementary Information) [43]. The SDF for the scalar interaction is then obtained numerically as the one-sided Fourier transform of $K(t)$:

$$J_{SC,Num.}(\omega_e) = Re\left\{ \int_0^{+\infty} K(t)\exp(-i\omega_e t)dt \right\}. \tag{17}$$

Both Eq. 16 and Eq. 17 can be calculated numerically from the traces $A_{iso,m}(t)$. An example of an SDF calculated with this procedure is shown in Fig. 2d. Within this formalism, the nuclear relaxation via scalar interaction is $R_{1,SC}^{(Num.)} = 6 \cdot J_{SC,Num.}(\omega_e)$. The demonstration is not obvious and has been reported previously in Ref. [40] and [43], and reviewed in the Supplementary Information.

## 3. The case of CHCl₃

Chloroform (CHCl₃) is extensively used as a target molecule for ¹³C-DNP experiments at both low and high magnetic fields [13,20,25,53,54]. CHCl₃ doped with nitroxide radicals is characterized by large scalar enhancements (i.e. positive) in the field range 0.32-14.1 T: notably, we recall a factor of 320-fold measured at 9.4 T [13], and a factor of 70-fold measured at 14.1 T [12]. Besides the enhancements, the coupling factor $\xi_{CHCl_3}$ has been reported for the system CHCl₃/TEMPONE over a 10 T field range [13,20,30]. This large data availability makes CHCl₃ an optimal model system for analyzing the details of the scalar interaction that drives ¹³C-DNP.

To better understand the molecular origin of the fluctuations of the scalar interaction, we simulated the dynamics of TEMPONE radical in CHCl₃ and reconstructed the SDF $J_{SC}(\omega_e)$ from the traces $A_{iso}(t)$. The dynamics of the TEMPONE radical in CHCl₃ were probed by MD simulations using GROMACS 2018.4 [55] and a set of previously reported parameters for nitroxide radicals [56]. The MD run was recorded for 10 ns with a resolution of 0.2 ps (Supplementary Information). For each snapshot, the hyperfine coupling $A_{iso}$ to the chloroform C atoms was calculated with DFT using Orca 4.2.1 [57,58] with BLYP as functional, EPR-II basis set for H, C, N, O atoms, and IGLO-II basis set for Cl [52]. Because the Fermi contact interaction is effective at short range (<10 Å), we included in the DFT calculations for each snapshot only the three CHCl₃ molecules closest to the radical, while $A_{iso}$ was set to 0 for the other molecules. As a result, we obtained one trace $A_{iso,m}(t)$ for each $m$ molecule of CHCl₃ in the simulation box.

We analyzed the $A_{iso,m}(t)$ traces calculated in the intervals 0–100 ps and 1000–2000 ps, and the same conclusions can be drawn from both datasets. Of the 1348 $A_{iso,m}(t)$ traces recorded, only a fraction have $A_{iso} \neq 0$ for at least one time point, i.e. 26 in the time interval 0–100 ps (Fig. 3a-b) and 154 in the longer interval 100–2000 ps. The values of $A_{iso}$ are mostly positive, with maxima $\sim 20$ MHz, while the negative ones are

$\lesssim 2$ MHz, in absolute value (Fig. 3a-b).

The traces show a fast modulation of $A_{iso}$, recognizable by the sharp peaks (Fig. 3). About 12% of the molecules with $A_{iso} \neq 0$ show a longer interaction (20 ps or more) and, on average, larger $A_{iso}$ values, and larger $K_m(t)$ (Fig. 3 and Supplementary Information). The rest of the CHCl$_3$ molecules have sporadic interactions with the radical, meaning that the elapsed time between the first and the last contact is not longer than 10 ps, and after that the molecule diffuses away from the radical ($A_{iso} = 0$).

This situation is reflected in the total autocorrelation function $K(t)$ (Fig. 4a): $K(t)$ has a maximum at $t<1$ ps, then non-negligible components in the interval $t = 1\text{–}50$ ps, and finally $K(t) \sim 0$ for $t> 100$ ps, meaning that the $A_{iso}$ does not fluctuate on such long timescales. The function $K(t)$ can be fitted with a sum of four exponential decays $\sum_{i=1}^{4} x_i \exp(-t/t_i)$. By performing the same analysis on five different portions of the MD trace, each 1 ns long, we found that the contributions that have larger weights $w_i$ have time constants $t_i = 0.1\text{–}25$ ps, while a longest one ($t_i > 100$ ps) has a weight that is almost one order of magnitude smaller than the others (Supplementary Information). Therefore, we can conclude that the hyperfine coupling $A_{iso}$ fluctuates mostly on the timescales 0.1–25 ps. The scalar SDF $J_{SC,Num.}(\omega_e)$ is computed numerically with Eq. 17 from the autocorrelation function $K(t)$ or from its fit function, the results are similar for all the portions of the traces that were analyzed (Supplementary Information). The results in Fig. 4b show a large discrepancy between the two curves in the region $B > 10$ T. This is a consequence of the sampling rate of the autocorrelation function, which is 0.2 ps for the numerical $K(t)$, and 0.05 ps for its analytical fit.

The geometry of CHCl$_3$/TEMPONE at three time points is shown in Fig. 5. The molecule that has the longer interaction with the radical (>20 ps) is in a hydrogen bond-like complex [59]. This interaction also leads to the largest $A_{iso}$ values recorded for the C atom. The other two closest molecules included in the calculation are more likely to interact with the radical via the Cl atom, leading to short and sporadic spikes in the $A_{iso}(t)$ traces (Fig. 5).

Previous $^{13}$C-DNP studies on CHCl$_3$ and CCl$_4$ suggested that the hydrogen bond-like interaction between CHCl$_3$ and radical may reduce the probability of short timescale modulation of $A_{iso}$, which is more effective in driving the polarization transfer at high magnetic fields [13,20]. This was supported by the observation of larger $^{13}$C enhancements on CCl$_4$ than on CHCl$_3$ at magnetic fields > 3 T [13,20]. However, here we note that, even during the formation of the transient complex, $A_{iso}(t)$ is still modulated on a $\lesssim 1$ ps time scale (Fig. 3 and 5 a). This means that the presence of a transient interaction between radical and target molecule does not prevent fast fluctuations of $A_{iso}$. A similar mechanism has been proposed very recently for interpreting scalar enhancements at high fields [31].

This numerical analysis can be compared with what has been previously obtained analytically with semi-classical nuclear relaxation theory [13,20]. In particular, the coupling factor data $\xi_{CHCl_3}$ in the range 0.34–9.4 T has been simulated with Eq. 5, using the scalar SDF given by the pulse model (Eq. 8) [13]. The latter was assumed to be a sum of two components (i.e. two types of collision):

$$
\begin{aligned}
J_{SC,Pulse}^{CHCl_3}(\omega_e) &= J_{SC}^{(1)}(\omega_e, \tau_1) + J_{SC}^{(2)}(\omega_e, \tau_2) = \\
&= \frac{4\pi^2 \langle A_1 \rangle^2}{\tau_{p,1}} [\tau_1 \exp(-\tau_1 \omega_e)]^2 + \\
&+ \frac{4\pi^2 \langle A_2 \rangle^2}{\tau_{p,2}} [\tau_2 \exp(-\tau_2 \omega_e)]^2 .
\end{aligned}
\tag{18}
$$

The experimental $\xi_{CHCl_3}$ has been simulated with Eq. 5 and the parameters in Table 1 obtained from a previous analysis [13]. Here we considered values of collisional correlation times in the ranges $2\tau_1 = 0.8\text{-}1.7$ ps and $2\tau_2 = 16\text{–}40$ ps (Fig. 6a). Supported by a comparative analysis of $\xi$ in CCl$_4$ [13,20], the collision characterized by the long $\tau_2$ was previously attributed to an hydrogen bond-like interaction between the radical and the CHCl$_3$ molecule. On the contrary, the faster collisions ($2\tau_1 \sim 1$ ps) were associated to random elastic collisions,

possibly favored by the halogen (Cl). Notably, this description of the electron-nuclear scalar interaction based on phenomenological arguments agrees very well with the dynamical features identified here with MD/DFT simulations. The correlation times $2\tau_1 = 0.8\text{-}1.7$ ps and $2\tau_2 = 16\text{–}40$ ps are close to the time constants extracted from the traces calculated numerically (Fig. 3 and 4), i.e. $t_i \sim 0.1\text{–}20$ ps.

A quantitative comparison between the two models is shown in Fig. 6b, which displays the scalar terms $k_{SC} J_{SC}(\omega_e, \tau_{SC})$ and the dipolar terms $5k_D J_D(\omega_e, \tau_D)$, whose difference gives the coupling factor (Eq. 5). While the ratio between scalar and dipolar is found to be model independent, the curves have been rescaled to maximum overlap to account for the concentration of the radical, which is taken into account differently in the different models. The scalar SDF $J_{SC,Pulse}^{CHCl_3}(\omega_e)$ calculated with the phenomenological pulse model (Eq. 18) and the numerically calculated $J_{SC,Num.}(\omega_e)$ agree very well in the field range 0.3–10 T. The high field region (B>10 T) is more problematic: on the one hand, the pulse model (Eq. 18) does not have a third component $\tau_3 \ll 1$ ps, because it is not necessary to explain the data up to 9.4 T; on the other hand, the numerical simulations performed with a resolution of 0.2 ps could not provide sufficient insight into the higher frequency regime. For the dipolar part, we compared the hard-sphere force free model that describes the dipole-dipole coupling arising from the translational diffusion (Supplementary Information) with $J_D(\omega_e)$ calculated by Sezer and coworkers from MD simulations [52]. In this case too, the two models give comparable results.

A similar analysis of the coupling factor $\xi_{CHCl_3}$ and the underlying scalar interaction can be performed using the BRW relaxation theory. To this aim, we computed numerically the relaxation superoperator $\widehat{\widehat{R}}$ with *Spinach* [60] for an electron-$^{13}$C spin pair interacting via dipole-dipole coupling (rotational dynamics) and scalar relaxation of the first kind (collisional dynamics). One can demonstrate that the coupling factor $\xi$ in the Liouville space formalism is (Supplementary Information):

$$
\xi \sim \frac{\sigma}{R_{1,n}} = \frac{\langle \widehat{N}_z | \widehat{\widehat{R}} | \widehat{E}_z \rangle}{\langle \widehat{N}_z | \widehat{\widehat{R}} | \widehat{N}_z \rangle}
\tag{19}
$$

where $\sigma$ is the cross-relaxation rate between the electron and nuclear spins, and $R_{1,n}$ is the longitudinal nuclear relaxation rate. The field dependence of $\xi_{CHCl_3}$ was simulated numerically with Eq. 19 and the set of parameters in Table 1. As shown in Fig. 6a, the data are well reproduced when the scalar contribution is parametrized with two contributions with correlation times $\tau_1 = 0.8$ ps and $\tau_1 = 30$ ps, respectively. These results are consistent with the analysis presented above. The comparison of the scalar SDFs (Fig. 6b) shows that the use of a sum of exponential decays as autocorrelation function is a good approximation of the phenomenological pulse model, which better represents the collisional dynamics of the radical/target molecule pair. The dipolar SDF calculated with the BRW theory uses a dipole-dipole coupling arising from isotropic rotational diffusion, and therefore deviates from the translational diffusion computed by the phenomenological model. This does not affect significantly the predictions of the coupling factor, but can be improved by taking into account the coupling between rotational and translational diffusion.

## 4. Conclusions and outlook

In summary, we have presented three models (phenomenological relaxation theory, numerical BRW treatment, and MD/DFT simulations) to describe the electron-nuclear scalar cross-relaxation that drives the polarization transfer in the liquid state. These three approaches give consistent results when analyzing $^{13}$C-DNP data obtained in the model system CHCl$_3$ and TEMPONE radical, and can describe the same complex collisional dynamics. Although the numerical MD/DFT simulation offers greater insight into the details of molecular interactions, modeling the experimental data with relaxation theory leads to a correct estimate of the timescale at which the electron-nuclear hyperfine coupling is

**Table 1**

Parameters used for the simulations of $\xi_{CHCl_3}$ as a function of the magnetic field with the phenomenological relaxation model and with the BRW numerical simulation. [1]The Pulse model (Eq. 18) requires the collision frequencies $1/\tau_{p,i}$ in the prefactors, and those are $\tau_{p,1} = \tau_{p,2} = 50$ps.

| | Phenom. relaxation model | | | | WRB theory | | | | |
|---|---|---|---|---|---|---|---|---|---|
| | $\langle A_1 \rangle$ (MHz)[1] | $2\tau_1$ (ps) | $\langle A_2 \rangle$ (MHz)[1] | $2\tau_2$ (ps) | $\Delta_a$ (MHz) | $w_1$ | $\tau_1$ (ps) | $w_2$ | $\tau_2$ (ps) |
| Scalar interaction | 0.67 | 0.8-1.4 | 0.19 | 16–40 | 3.6 | 0.38 | 0.5-1.7 | 0.62 | 18–38 |
| | $r_d^H$ (Å) | $\tau_D^H$ (ps) | $r_d^{Cl}$ (Å) | $\tau_D^{Cl}$ (ps) | $r$ (Å) | $\tau$ (ps) | | | |
| Dipolar interaction | 3.4 | 39 | 4.0 | 53 | 3.1 | 30 | | | |
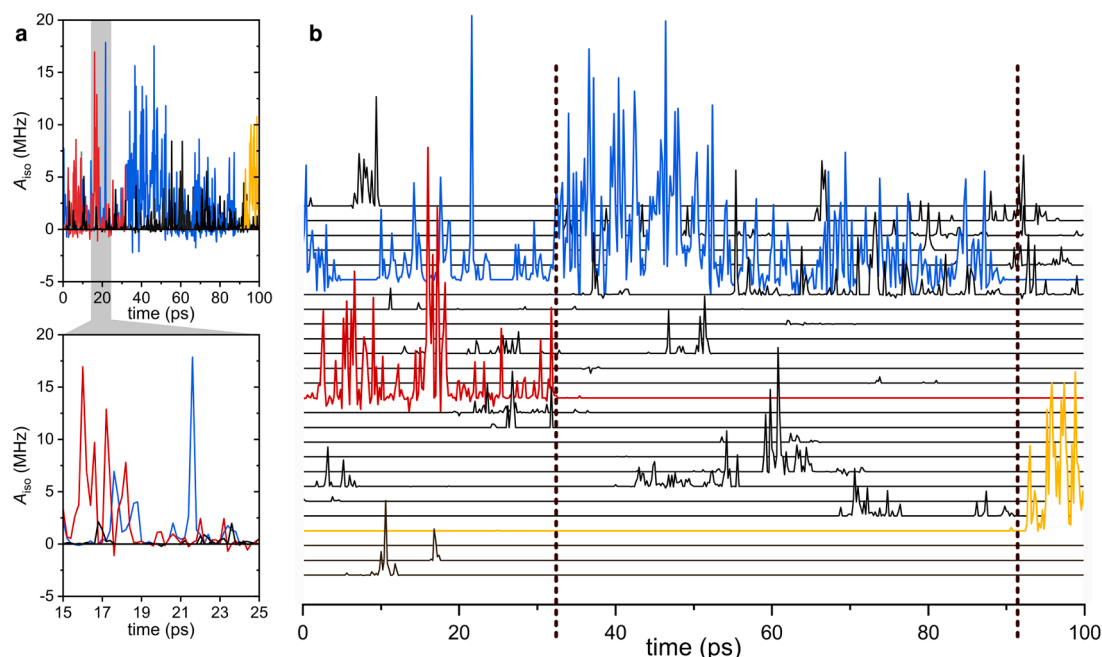


**Fig. 3. a)** Time dependence $A_{iso,m}(t)$ of the hyperfine coupling between the $^{13}C$ of $CHCl_3$ and the unpaired electron of the nitroxide radical calculated from MD/DFT simulations (time resolution 0.2 ps). The traces were recorded in the time interval 0–100 ps: of the total 1348 traces here we show the 26 traces that have $A_{iso}(t) \neq 0$ for at least one time point. **b)** Same $A_{iso,m}(t)$ traces displayed in a stacked plot. The dashed lines mark the time points when the H-bond-like complex jumps from one $CHCl_3$ molecule to the other. The traces of the molecules that form a long (>20 ps) transient complex with the nitroxide radical are highlighted in colors.
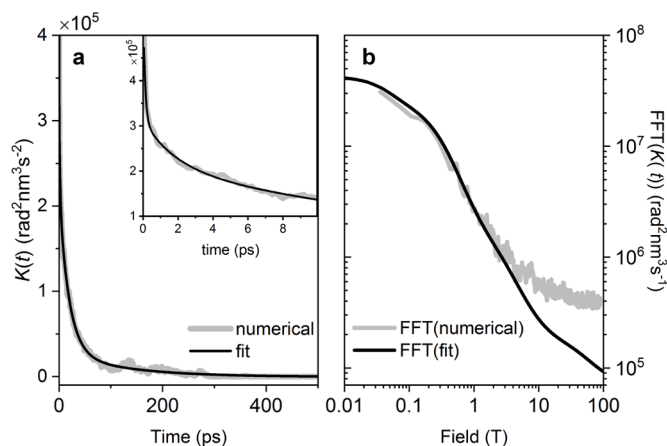


**Fig. 4. a)** Autocorrelation function $K(t) = \sum_m K_m(t)$ calculated for the traces $A_{iso,m}(t)$ in the time interval 1000–2000 ps with a sampling of 0.2 ps. The fit of $K(t)$ was performed with a sum of four exponential decays with a sampling of 0.05 ps. **b)** Numerical Fourier transform of the autocorrelation function $K(t)$ (gray) and of its multi-exponential fit (black).

modulated. Concerning the molecular origin of these fluctuations, the existence of transient radical/target molecule complex (persisting for 20–40 ps) does not exclude the presence of additional faster dynamics

($\lesssim 1$ ps), which can be effective for scalar relaxation at high magnetic field. A similar type of dynamics has been recently proposed in a comprehensive study at 9.4 T [31] and can be responsible for scalar-dominated $^{13}C$-DNP enhancements that have been observed at high field in non-halogenated compounds [12,13,20]. We expect that $^{13}C$-DNP in the liquid state driven by the scalar mechanism could be effective for a large variety of compounds, broadening the scope of the method. In this context, both models based on relaxation theory and numerical MD/DFT calculation offer robust tools to quantitatively investigate the details of the scalar cross-relaxation mechanisms.

*Author contributions statement*

T.O. conceived the study; M.H. performed MD/DFT calculations; I.K. provided new tools for simulations with *Spinach* and wrote the initial simulation routine; T.O. performed the simulation with *Spinach*, analyzed all the data and wrote the paper. All authors discussed the results and contributed to the writing of the manuscript.

*Declaration of competing interests*

The authors declare that they have no known competing financial interests or personal relationships that could have appeared to influence the work reported in this paper.
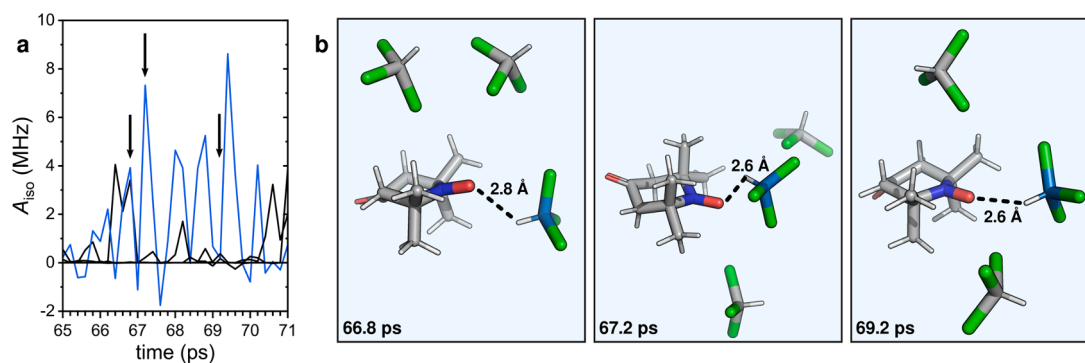
**Fig. 5. a)** Traces $A_{\mathrm{iso}}(t)$ plotted over 6 ps (color code from Fig. 3). **b)** Geometries of the TEMPONE and the closest three CHCl$_3$ molecules a three different time points, indicated by the arrows in panel a. The closest C atom is color coded as the trace in panel a and in Fig. 3 (atom color code: H white; C gray; N blue; O red; Cl green). Graphics and distances were obtained with Pymol. (For interpretation of the references to colour in this figure legend, the reader is referred to the web version of this article.)
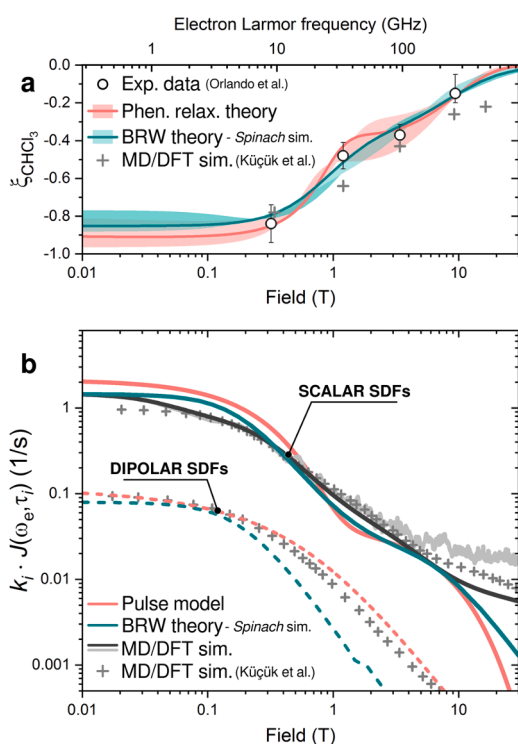


**Fig. 6. a)** Experimental and simulated $^{13}$C coupling factor $\xi_{\mathrm{CHCl_3}}$ as a function of the field for CHCl$_3$ doped with TEMPONE radical. Experimental data are from Ref. [13]. Simulations were performed with the semi-classical relaxation theory and with the full BRW treatment with *Spinach* using the parameters from Table 1, which include a distribution of collisional times (shaded area). The best agreement (solid lines) was obtained with $2\tau_1 = 0.5$ ps and $2\tau_1 = 24$ ps for the semi-classical model and $2\tau_1 = 0.8$ ps and $2\tau_1 = 30$ ps for the full BRW treatment. The coupling factor calculated with numerical simulations (MD/DFT) is from Ref. [52]. **b)** Scalar and dipolar SDFs from the models used to simulate the coupling factor $\xi_{\mathrm{CHCl_3}}$. For the MD/DFT calculations, we report both the SDFs from Fig. 4b. The curves from different models have been rescaled to the maximum overlap to account for scaling factor due to the radical concentration, which is included differently in the three models. Importantly, the ratio scalar to dipolar is model independent.

## Acknowledgments

discussions.

## Supplementary material

Supplementary material associated with this article can be found, in the online version, at 10.1016/j.jmro.2022.100040

## References

[1] J.H. Ardenkjaer-Larsen, G.S. Boebinger, A. Comment, S. Duckett, A.S. Edison, F. Engelke, C. Griesinger, R.G. Griffin, C. Hilty, H. Maeda, G. Parigi, T.F. Prisner, E. Ravera, P.J. van Bentum, S. Vega, A. Webb, C. Luchinat, H. Schwalbe, L. Frydman, Facing and overcoming sensitivity challenges in biomolecular NMR spectroscopy, Angewandte Chemie - International Edition 54 (32) (2015) 9162–9185, https://doi.org/10.1002/anie.201410653.

[2] G. Jeschke, L. Frydman, Nuclear hyperpolarization comes of age, Journal of Magnetic Resonance 264 (2016) 1–2, https://doi.org/10.1016/j.jmr.2016.01.020. http://linkinghub.elsevier.com/retrieve/pii/S1090780716000768

[3] T. Wenckenbach, Essentials of Dynamic Nuclear Polarization, Spindrift Publications, The Netherlands, 2016.

[4] K. Kundu, F. Mentink-Vigier, A. Feintuch, S. Vega, DNP Mechanisms, eMagRes 8 (3) (2019) 295–338, https://doi.org/10.1002/9780470034590.emrstm1550.

[5] B. Corzilius, High-field dynamic nuclear polarization, Annual Reviews of Physical Chemistry 71 (2020) 7.1–7.28.

[6] P. Berruyer, L. Emsley, A. Lesage, DNP In materials science: touching the surface, eMagRes 7 (4) (2018) 93–104, https://doi.org/10.1002/9780470034590. emrstm1554.

[7] V.P. Denysenkov, T.F. Prisner, Liquid-state overhauser DNP at high magnetic fields, eMagRes 8 (1) (2019) 41–54, https://doi.org/10.1002/9780470034590. emrstm1557.

[8] V. Denysenkov, T.F. Prisner, Liquid state dynamic nuclear polarization probe with fabry-Perot resonator at 9.2 t, Journal of Magnetic Resonance 217 (2012) 1–5, https://doi.org/10.1016/j.jmr.2012.01.014.

[9] P. Neugebauer, J.G. Krummenacker, V.P. Denysenkov, G. Parigi, C. Luchinat, T. F. Prisner, Liquid state DNP of water at 9.2 t: an experimental access to saturation, Physical Chemistry Chemical Physics 15 (2013) 6049–6056, https://doi.org/10.1039/c3cp44461a.

[10] D. Yoon, A.I. Dimitriadis, M. Soundararajan, C. Caspers, J. Genoud, S. Alberti, E. de Rijk, J.-P. Ansermet, High-Field liquid-State dynamic nuclear polarization in microliter samples, Analytical chemistry 90 (2018) 5620–5626, https://doi.org/10.1021/acs.analchem.7b04700.

[11] T. Dubroca, A.N. Smith, K.J. Pike, S. Froud, R. Wylde, B. Trociewitz, J. McKay, F. Mentink-Vigier, H. van Tol, S. Wi, W. Brey, J.R. Long, L. Frydman, S. Hill, A quasi-optical and corrugated waveguide microwave transmission system for simultaneous dynamic nuclear polarization NMR on two separate 14.1 T spectrometers, Journal of Magnetic Resonance 289 (2018) 35–44, https://doi.org/10.1016/j.jmr.2018.01.015.

[12] T. Dubroca, S. Wi, J. Van Tol, L. Frydman, S. Hill, Large volume liquid state scalar overhauser dynamic nuclear polarization at high magnetic field, Physical Chemistry Chemical Physics 21 (38) (2019) 21200–21204, https://doi.org/10.1039/c9cp02997d.

[13] T. Orlando, R. Dervişoğlu, M. Levien, I. Tkach, T.F. Prisner, L.B. Andreas, V. P. Denysenkov, M. Bennati, Dynamic nuclear polarization of $^{13}$c nuclei in the liquid state over a 10 tesla field range, Angewandte Chemie - International Edition 58 (5) (2019) 1402–1406, https://doi.org/10.1002/anie.201811892.

[14] C. Griesinger, M. Bennati, H.M. Vieth, C. Luchinat, G. Parigi, P. Höfer, F. Engelke, S.J. Glaser, V. Denysenkov, T.F. Prisner, Dynamic nuclear polarization at high magnetic fields in liquids, Progress in nuclear magnetic resonance spectroscopy 64 (2012) 4–28, https://doi.org/10.1016/j.pnmrs.2011.10.002.

[15] P.J. van Bentum, G.H.A. van der Heijden, J.A. Villanueva-Garibay, A.P. Kentgens, Quantitative analysis of high field liquid state dynamic nuclear polarization, Physical Chemistry Chemical Physics 13 (39) (2011) 17831, https://doi.org/10.1039/c1cp22002k.http://xlink.rsc.org/?DOI=c1cp22002k

[16] M. Gafurov, V. Denysenkov, M.J. Prandolini, T.F. Prisner, Temperature dependence of the proton overhauser DNP enhancements on aqueous solutions of Fremy's salt measured in a magnetic field of 9.2 T, Applied magnetic resonance 43 (1–2) (2012) 119–128, https://doi.org/10.1007/s00723-012-0352-7.

[17] T.F. Prisner, V.P. Denysenkov, D. Sezer, Liquid state DNP at high magnetic fields: instrumentation, experimental results and atomistic modelling by molecular dynamics simulations, Journal of Magnetic Resonance 264 (2016) 68–77, https://doi.org/10.1016/j.jmr.2015.11.004.

[18] N.M. Loening, M. Rosay, V. Weis, R.G. Griffin, Solution-state dynamic nuclear polarization at high magnetic field, Journal of the American Chemical Society 124 (30) (2002) 8808–8809, https://doi.org/10.1021/ja026660g.

[19] C. George, N. Chandrakumar, Chemical-shift-resolved $^{19}$f nmr spectroscopy between 13.5 and 135 MHz: overhauser-DNP-enhanced diagonal suppressed correlation spectroscopy, Angewandte Chemie 126 (32) (2014) 8581–8584, https://doi.org/10.1002/anie.201402320.

[20] G. Liu, M. Levien, N. Karschin, G. Parigi, C. Luchinat, M. Bennati, One-thousand-fold enhancement of high field liquid nuclear magnetic resonance signals at room temperature, Nature chemistry 9 (2017) 676–680, https://doi.org/10.1038/nchem.2723.

[21] M. Bennati, T. Orlando, Overhauser DNP in liquids on $^{13}$c nuclei, eMagRes 8 (1) (2019) 11–18, https://doi.org/10.1002/9780470034590.emrstm1581.

[22] M.G. Concilio, M. Soundararajan, L. Frydman, I. Kuprov, High-field solution state DNP using cross-correlations, Journal of Magnetic Resonance 326 (2021) 106940, https://doi.org/10.1016/j.jmr.2021.106940.

[23] M.G. Concilio, I. Kuprov, L. Frydman, J-driven dynamic nuclear polarization for sensitizing high field solution state NMR, Physical Chemistry Chemical Physics 24 (2022) 2118–2125, https://doi.org/10.1039/D1CP04186J.

[24] M. Levien, M. Hiller, I. Tkach, M. Bennati, T. Orlando, Nitroxide derivatives for dynamic nuclear polarization in liquids: the role of rotational diffusion, The journal of physical chemistry letters 11 (2020) 1629–1635, https://doi.org/10.1021/acs.jpclett.0c00270.

[25] M. Levien, M. Reinhard, M. Hiller, I. Tkach, M. Bennati, T. Orlando, Spin density localization and accessibility in organic radicals for liquid-state DNP efficiency, Physical Chemistry Chemical Physics 23 (2021) 4480–4485, https://doi.org/10.1039/d0cp05796g.

[26] W. Müller-Warmuth, K. Meise-Gresch, Molecular Motions and Interactions as Studied by Dynamic Nuclear Polarization (DNP) in Free Radical Solutions volume 11, Academic Press, Inc., 1983, https://doi.org/10.1016/B978-0-12-025511-5.50007-4.

[27] S. Stevenson, T. Glass, H.C. Dorn, $^{13}$C dynamic nuclear polarization: an alternative detector for recycled-Flow NMR experiments, Analytical chemistry 70 (13) (1998) 2623–2628, https://doi.org/10.1021/ac971337v.

[28] M.D. Lingwood, S. Han, Dynamic nuclear polarization of $^{13}$c in aqueous solutions under ambient conditions, Journal of Magnetic Resonance 201 (2) (2009) 137–145, https://doi.org/10.1016/j.jmr.2009.09.002.

[29] W. Müller-Warmuth, R. Vilhjalmsson, P. Gerlof, J. Smidt, J. Trommel, Intermolecular interactions of benzene and carbon tetrachloride with selected free radicals in solution as studied by $^{13}$c and $^{1}$h dynamic nuclear polarization, Molecular physics 31 (4) (1976) 1055–1067, https://doi.org/10.1080/00268977600100811.

[30] X. Wang, W.C. Isley III, S.I. Salido, Z. Sun, L. Song, K.H. Tsai, C.J. Cramer, H. C. Dorn, Optimization and prediction of the electron- nuclear dipolar and scalar interaction in $^{1}$h and $^{13}$c liquid state dynamic nuclear polarization, Chemical Science 6 (2015) 6482–6495, https://doi.org/10.1039/c5sc02499d.

[31] D. Dai, X. Wang, V. Denysenkov, X. He, Y. Liu, X.-l. Yang, C. Glaubitz, T. Prisner, J. Mao, Room-temperature dynamic nuclear polarization enhanced NMR spectroscopy of small biological molecules in water, Nature communications 12 (2021) 6880, https://doi.org/10.1038/s41467-021-27067-0.

[32] A.G. Redfield, On the theory of relaxation processes, IBM Journal of Research and Development 1 (1) (1957) 19–31, https://doi.org/10.1147/rd.11.0019.

[33] R.K. Wangsness, F. Bloch, The dynamical theory of nuclear induction, The Physical review 89 (1953) 728–739, https://doi.org/10.1103/PhysRev.89.728.

[34] A.W. Overhauser, Polarization of nuclei in metals, Physical Review 92 (2) (1953) 411–415, https://doi.org/10.1103/PhysRev.92.411.

[35] I. Solomon, Relaxation processes in a system of two spins, Physical Review 99 (2) (1955) 559–565, https://doi.org/10.1103/PhysRev.99.559.

[36] K.H. Hausser, D. Stehlik, Dynamic nuclear polarization in liquids, in: J.S. Waugh (Ed.), Advances in Magnetic Resonance volume 3, Academic Press, 1968, pp. 79–139, https://doi.org/10.1016/9781849730877-00155.

[37] M. Bennati, C. Luchinat, G. Parigi, M.T. Türke, Water $^{1}$h relaxation dispersion analysis on a nitroxide radical provides information on the maximal signal enhancement in overhauser dynamic nuclear polarization experiments, Physical Chemistry Chemical Physics 12 (22) (2010) 5902–5910, https://doi.org/10.1039/c002146f.

[38] L.-P. Hwang, J.H. Freed, Dynamic effects of pair correlation functions on spin relaxation by traslational diffusion in liquids, The Journal of chemical physics 63 (9) (1975) 4017–4025.

[39] J.H. Freed, Dynamic effects of pair correlation functions on spin relaxation by translational diffusion in liquids. II. finite jumps and independent $t_1$ processes, The Journal of chemical physics 68 (9) (1978) 4034–4037.

[40] D. Sezer, M.J. Prandolini, T.F. Prisner, Dynamic nuclear polarization coupling factors calculated from molecular dynamics simulations of a nitroxide radical in water, Physical Chemistry Chemical Physics 11 (31) (2009) 6626–6637, https://doi.org/10.1039/b905709a.

[41] D. Sezer, Computation of DNP coupling factors of a nitroxide radical in toluene: seamless combination of MD simulations and analytical calculations, Physical Chemistry Chemical Physics 15 (2) (2013) 526–540, https://doi.org/10.1039/c2cp42430d.

[42] D. Sezer, Rationalizing overhauser DNP of nitroxide radicals in water through MD simulations, Physical Chemistry Chemical Physics 16 (2014) 1022–1032, https://doi.org/10.1039/c3cp53565g.

[43] S.E. Küçük, T. Biktagirov, D. Sezer, Carbon and proton overhauser DNP from MD simulations and ab initio calculations: TEMPOL in acetone, Physical Chemistry Chemical Physics 17 (38) (2015) 24874–24884, https://doi.org/10.1039/c5cp04405g.

[44] J.R. Biller, H. Elajaili, V. Meyer, G.M. Rosen, S.S. Eaton, G.R. Eaton, Electron spin-lattice relaxation mechanisms of rapidly-tumbling nitroxide radicals, Journal of Magnetic Resonance 236 (2013) 47–56, https://doi.org/10.1016/j.jmr.2013.08.006.

[45] N. Enkin, G. Liu, M. del Carmen Gimenez-Lopez, K. Porfyrakis, I. Tkach, M. Bennati, A high saturation factor in overhauser DNP with nitroxide derivatives: the role of $^{14}$n nuclear spin relaxation, Physical Chemistry Chemical Physics 17 (2015) 11144–11149, https://doi.org/10.1039/C5CP00935A.

[46] A. Abragam, The principles of nuclear magnetism, in: International series of monographs on physics, Clarendon Press, Oxford, 1989.

[47] F. Noack, G.J. Krüger, W. Müller-Warmuth, R. Van Steenwinkel, Stochastische prozesse in spinsystemen, Zeitschrift fur Naturforschung - Section A Journal of Physical Sciences 22 (12) (1967) 2102–2108, https://doi.org/10.1515/zna-1967-1239.

[48] G. Parigi, E. Ravera, M. Bennati, C. Luchinat, Understanding overhauser dynamic nuclear polarisation through NMR relaxometry, Molecular physics 117 (7–8) (2019) 888–897, https://doi.org/10.1080/00268976.2018.1527409.

[49] I. Kuprov, D.M. Hodgson, J. Kloesges, C.I. Pearson, B. Odell, T.D.W. Claridge, Anomalous nuclear overhauser effects in carbon-Substituted aziridines: scalar cross-Relaxation of the first kind, Angewandte Chemie 127 (12) (2015) 3768–3772, https://doi.org/10.1002/ange.201410271.

[50] D.L. Goodwin, I. Kuprov, Auxiliary matrix formalism for interaction representation transformations, optimal control, and spin relaxation theories, The Journal of chemical physics 143 (8) (2015) 084113, https://doi.org/10.1063/1.4928978.

[51] E. Ravera, C. Luchinat, G. Parigi, Basic facts and perspectives of overhauser DNP NMR, Journal of Magnetic Resonance 264 (2016) 78–87, https://doi.org/10.1016/j.jmr.2015.12.013.

[52] S.E. Küçük, D. Sezer, Multiscale computational modeling of $^{13}$c dnp in liquids, Physical Chemistry Chemical Physics 18 (18) (2016) 9353–9357, https://doi.org/10.1039/c6cp01028h.

[53] H.C. Dorn, T.E. Glass, R. Gitti, K.H. Tsai, Transfer of 1H and 13c dynamic nuclear polarization from immobilized nitroxide radicals to flowing liquids, Applied magnetic resonance 2 (1) (1991) 9–27, https://doi.org/10.1007/BF03166265.

[54] M. Reese, M.T. Türke, I. Tkach, G. Parigi, C. Luchinat, T. Marquardsen, A. Tavernier, P. Höfer, F. Engelke, C. Griesinger, M. Bennati, $^{1}$H and $^{13}$c dynamic nuclear polarization in aqueous solution with a two-field (0.35 t/14 t) shuttle DNP spectrometer, Journal of the American Chemical Society 131 (42) (2009) 15086–15087, https://doi.org/10.1021/ja905959n.

[55] S. Pronk, S. Páll, R. Schulz, P. Larsson, P. Bjelkmar, R. Apostolov, M.R. Shirts, J. C. Smith, P.M. Kasson, D. van der Spoel, B. Hess, E. Lindahl, GROMACS 4.5: A high-throughput and highly parallel open source molecular simulation toolkit, Bioinformatics (Oxford, England) 29 (7) (2013) 845–854, https://doi.org/10.1093/bioinformatics/btt055.

[56] E. Stendardo, A. Pedone, P. Cimino, M. Cristina Menziani, O. Crescenzi, V. Barone, Extension of the amber force-field for the study of large nitroxides in condensed phases: an ab initio parameterization, Physical Chemistry Chemical Physics 12 (2010) 11697–11709, https://doi.org/10.1039/C001481H.

[57] F. Neese, The ORCA program system, Wiley Interdisciplinary Reviews: Computational Molecular Science 2 (1) (2012) 73–78, https://doi.org/10.1002/wcms.81.

[58] F. Neese, Software update: the orca program system, version 4.0, WIREs Computational Molecular Science 8 (1) (2018) e1327, https://doi.org/10.1002/wcms.1327.

[59] M. Pavone, A. Sillanpää, P. Cimino, O. Crescenzi, V. Barone, Evidence of variable H-bond network for nitroxide radicals in protic solvents, Journal of Physical Chemistry B 110 (33) (2006) 16189–16192, https://doi.org/10.1021/jp063872h.

[60] H.J. Hogben, M. Krzystyniak, G.T. Charnock, P.J. Hore, I. Kuprov, Spinach - A software library for simulation of spin dynamics in large spin systems, Journal of Magnetic Resonance 208 (2) (2011) 179–194, https://doi.org/10.1016/j.jmr.2010.11.008.